Two-dimensional Ekman-Inertial Instability: A comparison with Inertial Instability

By

Fabiola Trujano-Jiménez[1] (fabiola.trujanojimenez@mail.utoronto.ca)

Varvara E. Zemskova[2,3] (bzemskov@uwaterloo.ca)

Nicolas Grisouard[1] (nicolas.grisouard@utoronto.ca)

[1] Department of Physics, University of Toronto, Toronto, ON M5S 1A7, Canada

[2] Department of Applied Mathematics, University of Waterloo, Waterloo, ON N2L 3G1, Canada

[3] College of Earth, Ocean, and Atmospheric Sciences, Oregon State University, Oregon 97331, USA

This paper is a non-peer reviewed preprint submitted to EarthArXiv. It was submitted to *Physical Review Fluids* for peer review on August 20th, 2024. If accepted for publication, the final version of this manuscript will be available via the *'Peer-reviewed Publication DOI'* link on the right-hand side of this webpage. Please feel free to contact any of the authors.

Two-dimensional Ekman-Inertial Instability: A comparison with Inertial Instability

Fabiola Trujano-Jiménez,[1] Varvara E. Zemskova,[2,3] and Nicolas Grisouard[1,*]

[1] *Department of Physics, University of Toronto, Toronto, ON M5S 1A7, Canada*

[2] *Department of Applied Mathematics, University of Waterloo, Waterloo, ON N2L 3G1, Canada*

[3] *College of Earth, Ocean, and Atmospheric Sciences, Oregon State University, Oregon 97331, USA*

(Dated: August 26, 2024)

Abstract

In the ocean, submesoscale flows tend to undergo several hydrodynamic instabilities. In particular, Inertial Instability (InI) and Ekman-Inertial Instability (EII) are known to develop in geostrophically balanced barotropic flows whose lateral shear is larger in magnitude and opposite in sign to the Coriolis parameter. Although these instabilities share some elements, their dynamical nature can lead to fundamental differences. However, the current analytical description of EII is one-dimensional, which makes it difficult to compare against InI in a more realistic scenario. To overcome this limitation, we conduct two-dimensional numerical simulations of both InI and EII in a submesoscale jet and explore the induced vertical flow, the growth rate, and the energetics of each instability. Furthermore, we investigate the sensitivity of our results to variations in the minimum Rossby number of the jet. We find that EII grows faster than InI and induces stronger vertical flow, especially near the surface. Both instabilities radiate inertial waves away from the current, and these waves predominantly propagate across the anticyclonic side of the jet. Finally, when the instabilities weaken, the fluid reaches a stable state that is remarkably similar in both cases. This study highlights the similarities and differences between InI and EII and provides further insight into the mechanism behind EII that makes it capable of outcompeting other submesoscale instabilities.

I. INTRODUCTION

The dynamics of the ocean are shaped by physical processes of different temporal and spatial scales, as well as by the complex interactions between them [1, 2]. In recent decades, special attention has been drawn to the submesoscale, an ocean scale characterized by flows with horizontal scales of $0.1 - 10$ km, vertical scales of $0.001 - 1$ km, and temporal scales of hours to days [3, 4]. The increasing availability of high-resolution computational models and remote sensing instruments led to the emergence of the submesoscale as a field of study and demonstrated its remarkable relevance in connecting larger scales such as the mesoscale and smaller scales such as the microscale.

Submesoscale flows induce relatively strong vertical velocities, making them essential for transporting momentum, heat, gases, and nutrients between the surface and the interior of

* nicolas.grisouard@utoronto.ca

the ocean [5–10]. For this reason, submesoscale flows play a crucial role not only in ocean dynamics, but also in the global climate system and the sustenance of marine life. Moreover, such intense vertical flows provide a path for dissipation of kinetic energy by transferring energy from large to small scales in a process known as a forward cascade of energy [3, 11, 12]. In the mesoscale, most of the kinetic energy is stored in the form of jets and eddies that are approximately in geostrophic and hydrostatic balance. Their kinetic energy tends to experience an inverse cascade, i.e., energy transfers from smaller to larger scales, and they tend to be robust to disturbances without experiencing significant dissipation. As such, submesoscale flows are proving to be an essential link to closing the kinetic energy budget of the ocean [13].

The submesoscale is characterized by Rossby numbers ($\mathrm{Ro} = \zeta/f$, where ζ is the vertical vorticity and f is the Coriolis parameter) of $O(1)$ [3, 14], which makes submesoscale flows particularly prone to becoming dynamically unstable. Several submesoscale instabilities occur in the upper ocean, especially in regions with strong lateral density gradients, such as fronts or filaments [15–22]. In particular, when submesoscale barotropic flows in geostrophic balance satisfy the condition $\mathrm{Ro} < -1$, small perturbations draw energy from the lateral shear of the flow and can grow enough to break the balance. This process is known as Inertial Instability (InI) and has been thought to play an important role in submesoscale dynamics [21, 23, 24]. In fact, linear stability analysis in infinite and uniform domains in the inviscid regime predicts that plane wave-like perturbations grow at a rate of $|f|\sqrt{-1-\mathrm{Ro}}$. Note that this type of analysis implicitly assumes that there is no interaction between different modes; in reality, such interactions could lead to much faster growth rates shortly after the onset of the instability [25].

Under the same conditions for InI development, along with the fact that the flow undergoes a sudden change in the surface wind stress, Grisouard and Zemskova [26] revealed the existence of what could be considered either a particular manifestation of InI, or a new submesoscale instability: the Ekman-Inertial Instability (EII). Similarly to InI, EII develops in submesoscale flows with $\mathrm{Ro} < -1$, and similarly to an Ekman layer, it is triggered by a tangential stress on the surface.

Despite the similarities previously described, there are several features that make EII a distinct instability capable of competing against and even grow faster than other common submesoscale instabilities. Indeed, one of the main differences between EII and InI is found in their respective triggering mechanisms. InI typically develops from perturbations in the interior of the flow, and hence, it is often described by vertical modes and studied using plane-wave linear stability analysis. In contrast, the perturbation that causes EII is a mismatch between surface and interior tangential stresses, which in turn propagates toward deeper layers of the flow via viscous tangential fluxes. This results in a very different growth rate for both instabilities. Namely, traditional linear stability analysis shows that InI grows exponentially, with the growth rate reduced by viscosity [e.g., 24, 27]. On the contrary, for a fluid layer at a given depth and a fast enough surface disturbance, EII exhibits a super-exponential growth rate in the first stage of its development when viscous stresses provide momentum from above. The EII growth rate then rapidly decreases and reaches a minimum below the inertial value, when said layer now provides momentum to the layer below. Eventually, the EII growth rate slowly tends toward the exponential growth rate of InI. As a result, a fundamental difference is found in the sources of energy and the effects of the turbulent viscosity in each instability. The only source of energy for InI is in the lateral shear of the flow, whereas viscous effects counteract its development throughout the entire process. On the contrary, in EII viscous stresses initially provide kinetic energy to a given layer of fluid, enhancing the development of EII during its early stages [26]. In later stages, viscous stresses then revert to their more standard behavior of slowing down the growth of the perturbations.

The analytical solution of Grisouard and Zemskova [26] for EII applies to a one-dimensional column of fluid. Consequently, this description neglects horizontal variations of the Rossby number, which implies an endless source of unstable flow since the Rossby number would indefinitely satisfy the condition $\mathrm{Ro} < -1$. In a more realistic scenario, as the instability develops, the Rossby number will vary across the flow, and the mixing of stable and unstable flow will eventually cause the instability to weaken and fade away. In order to account for this effect, an additional dimension must be included. This work aims to contribute to the overall understanding of submesoscale instabilities with a detailed analysis of the similarities and differences between EII and InI in a two-dimensional submesoscale current. The structure of this paper is as follows. In section II, we introduce the details of our numerical setup and the growth rate and energetics analysis performed on our data. Section III presents the results of a sample simulation, followed by a discussion on their sensitivity to variations in the Rossby number. We discuss the limitations of our study and summarize our findings in section IV.

II. METHODOLOGY

A. Numerical Setup

We set up a jet-like current of typical half-width $L = 1$ on an f-plane Cartesian ($\hat{\boldsymbol{x}}$, $\hat{\boldsymbol{y}}$, $\hat{\boldsymbol{z}}$, with $\hat{\boldsymbol{z}}$ pointing vertically upward) nondimensional domain of horizontal length $L_x = 16$ and height $H = 1$. The jet flows in the $\hat{\boldsymbol{y}}$ direction. Strictly speaking, the domain is two-and-a-half-dimensional, namely, there can be a non-zero velocity in the y-direction, but we set all y-derivatives to zero. This system is described by the equations of motion for a constant-density flow, which approximates the surface mixed layer. The unit time scale is the inverse of the Coriolis parameter $1/f = 1$. Then, the nondimensionalized equations of motion take the form

$$\frac{D\boldsymbol{v}}{Dt} + f\hat{\boldsymbol{z}} \times \boldsymbol{v} + \nabla\phi = \mathrm{Ek}\nabla^2\boldsymbol{v} \quad \text{and} \quad \nabla \cdot \boldsymbol{v} = 0, \tag{1}$$

where $\boldsymbol{v} = u\hat{\boldsymbol{x}} + v\hat{\boldsymbol{y}} + w\hat{\boldsymbol{z}}$ is the velocity field and its Cartesian components, ϕ is the deviation from hydrostatic pressure, and $\mathrm{Ek} = \nu/fH^2$ is the Ekman number, with ν the kinematic viscosity. Note that as mentioned above, $f = 1$ in our nondimensional unit system, but we keep its symbol to keep track of the Coriolis terms.

The initial state of the current is modeled as a Gaussian function given by

$$\boldsymbol{v}|_{t=0} = -v_0 \mathrm{e}^{-x^2/2}\hat{\boldsymbol{y}}, \tag{2}$$

where $v_0 = -\mathrm{Ro}_{\mathrm{min}}\mathrm{e}^{1/2}$ is the amplitude of the current. Note that $\mathrm{Ro}_{\mathrm{min}} = \min(\mathrm{Ro})$, with $\mathrm{Ro} = \partial_x v/f$ in our two-dimensional model.

We apply a constant wind stress τ in the direction of the initial current, that is,

$$\partial_z u|_{z=0} = 0 \quad \text{and} \quad \partial_z v|_{z=0} = \tau. \tag{3}$$

It is important to note that the numerical setup in both cases is almost identical; the only difference is in the value of the wind stress, with $\tau = 0$ in InI simulations and $\tau = 1$ in EII simulations.

Because the initial interior viscous stress is zero (no vertical shear of the initial current), the EII case is equivalent to a "step response", where the wind goes from zero to some finite value instantaneously at $t = 0$. The bottom boundary conditions, namely, at $z = -1$, for horizontal and vertical velocities are free-slip and rigid-lid, respectively. In the horizontal direction, we impose periodic boundary conditions.

We solve the equations of motion using Dedalus, a highly flexible computational framework suitable for optimal parallelized simulations that solves partial differential equations using spectral methods [28]. The computational domain consists of a Fourier basis with $n_x = 2048$ grid points in the horizontal direction and a Chebyshev basis with $n_z = 128$ grid points in the vertical direction. We use dealiasing scale factors of 3/2 for each axis. Our simulations use a fixed time step $\Delta t = 10^{-3}$ and a second-order, two-stage Runge-Kutta integrator. The total simulation time is $T_f = 40\pi$, that is, twenty inertial periods.

We conduct an analysis of the similarities and differences between InI and EII that result from variations in the minimum Rossby number, with $\mathrm{Ro}_{\min} \in \{-1.1, \ldots, -1.9\}$ increasing by 0.1 in each simulation. We keep the Ekman number constant, namely $\mathrm{Ek} = 10^{-3}$. Variations of this parameter would likely affect the vertical scale of each instability, but this work is focused on the comparison of other dynamical features.

B. Growth rate and energetics

We calculate the growth rate of the perturbations in each instability, namely,

$$\sigma = \frac{1}{2}\frac{1}{\langle w^2\rangle}\frac{d\langle w^2\rangle}{dt}, \tag{4}$$

where $\langle\cdot\rangle$ represents an integral over the full volume.

In a homogeneous fluid, the total kinetic energy $K = \langle|\boldsymbol{v}|^2/2\rangle$ is also the total energy of the system. To evaluate how much of the total energy is dissipated due to InI and EII, we calculate the energy budget of the flow, namely,

$$\frac{dK}{dt} = \underbrace{\mathrm{Ek}\left\langle\nabla^2(|\boldsymbol{v}|^2/2)\right\rangle}_{\text{Diffusion } \mathcal{D}} - \underbrace{\mathrm{Ek}\left\langle|\nabla\boldsymbol{v}|^2\right\rangle}_{\text{Dissipation } \varepsilon}, \tag{5}$$

where $\mathcal{D}$ and ε represent kinetic energy diffusion and dissipation, respectively. Note that because we calculate the energy budget over the full volume of the flow and owing to the boundary conditions, there is no contribution from the advective and pressure terms.

C. Inertial Oscillations

Initial adjustments in the presence of rotation trigger inertial oscillations of frequency f in the horizontal velocity field. These oscillations are homogeneous in space and therefore dissipate very little because of the absence of internal shear and of the free-slip boundary conditions at the bottom. In order to better visualize the flow that is solely induced by the development of InI and EII, we remove the signal of inertial oscillations by plotting data in the frame of reference of the volume mean flow and subtracting such mean from the horizontal velocity field. In other words, we define the mean along-x displacement as $\hat{x} = \int_0^t \langle u \rangle dt'$. Then, at each time step, we interpolate our data into a primed frame of reference defined by $x' = x - \hat{x}$. Finally, we subtract the mean flow that comprises the inertial oscillations from the horizontal velocity field to obtain $u' = u - \langle u \rangle$. Note that we only apply this procedure to facilitate the reading of certain plots in which inertial oscillations could obscure other features of interest.

Nevertheless, these inertial oscillations do not have any impact on σ, $\mathcal{D}$, and ε, and therefore, we use the full velocity fields to compute these quantities.

III. RESULTS

This section starts with a detailed analysis of a sample simulation characterized by $\mathrm{Ro}_{\mathrm{min}} = -1.5$. We select this value to allow for significant development of both InI and EII. Subsequently, we present our discussion around the effects on the dynamics and energetics of each instability resulting from variations of $\mathrm{Ro}_{\mathrm{min}}$, which is essentially the amplitude of the lateral shear of the initial current.

A. Sample case

1. Vertical Pumping

One of our main interests is the vertical velocity w induced by each instability, as it would be crucial for the vertical transport of physical properties in the ocean, particularly in the submesoscale. In Figure 1, we show snapshots of w at four different times that are selected to represent the onset, an intermediate stage, the weakening, and the return to a stable state

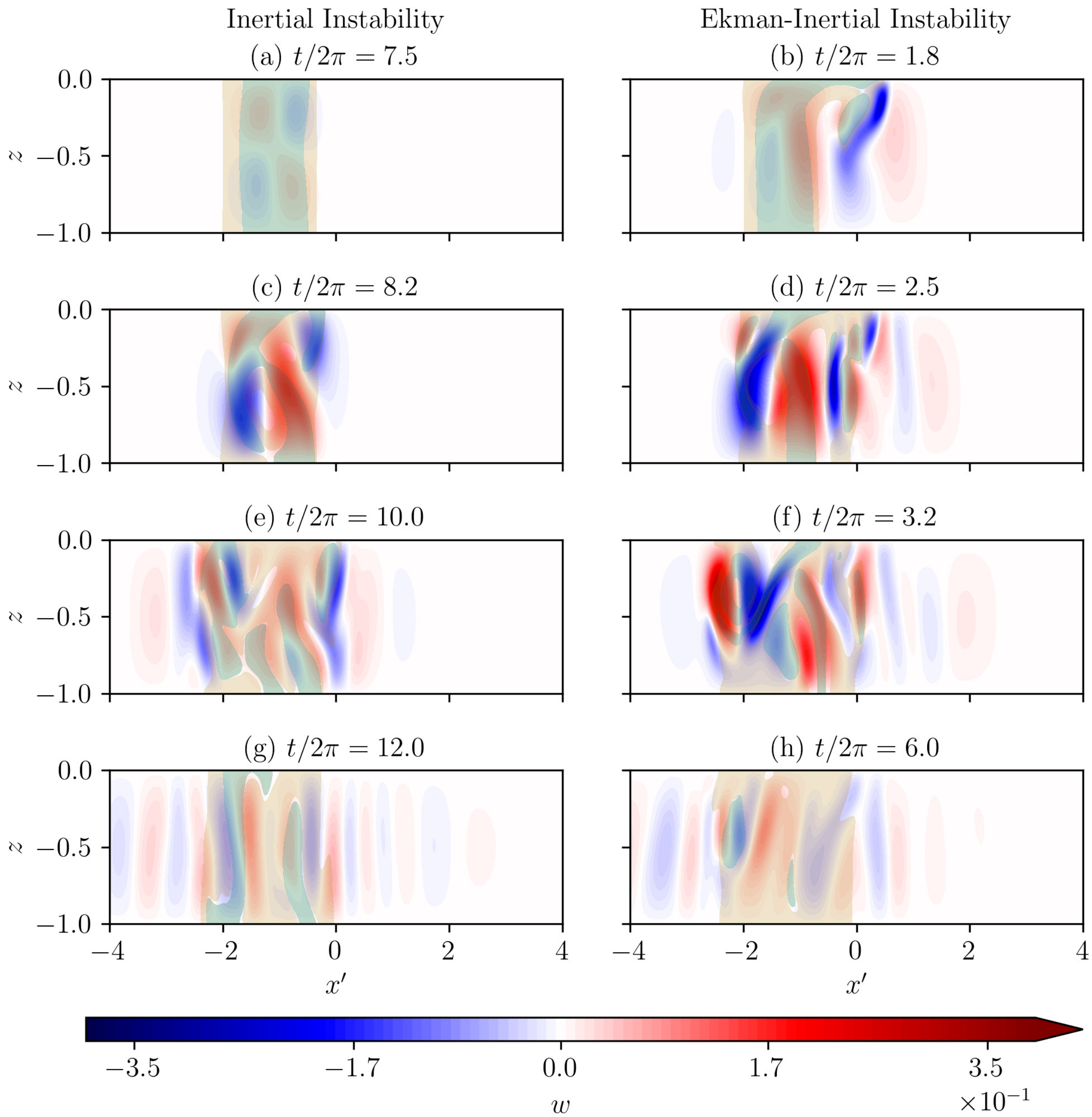

FIG. 1. Evolution of the vertical flow w (blue/red shades) induced by InI and EII at $\mathrm{Ro}_{\min} = -1.5$, visualized in the reference frame of the inertial oscillation. Translucent gold shades indicate marginally stable flow ($-0.99 < \mathrm{Ro} < -0.7$), and translucent turquoise indicate unstable flow ($\mathrm{Ro} < -1$).

of both InI and EII. Each panel also shows regions of marginally stable flow, where locally $-0.99 < \mathrm{Ro} < -0.7$, and unstable flow, where locally $\mathrm{Ro} < -1$. The contours of Ro seem to follow the structure of the vertical flow.

Several differences are immediately distinguishable. First, note from the time stamps that

EII takes significantly less time than InI to start and then reach its maximum development, which is a direct consequence of the much faster initiation and development of the instability. Furthermore, panels (a)–(d) show that the magnitude of the pumping induced by EII, hereafter called Ekman-Inertial pumping, is also larger than that of InI. In particular, panel (b) highlights that the Ekman-Inertial pumping is more intense near the surface, where the triggering stress is applied. We can also see from the gold and turquoise shades that fluid parcels closest to the surface are displaced the farthest, which is another distinctive feature of EII. On the other hand, the vertical flow induced by InI reaches its maximum values at deeper levels, namely around $z = -0.25$ and $z = -0.75$. The modal shape of this flow is particularly visible in the initial stage of InI shown in panel (a). Note from panels (e)–(h) that, at the end of both instabilities, wave packets are emitted away from the unstable regions.

To better visualize the time evolution of these waves, Figure 2 shows Hovmöller diagrams of w at $z = -0.5$. Despite the fact that Ekman-Inertial pumping is stronger near the surface, we found that the fundamental features of the flow do not change significantly across different depths, so we choose a common level for both instabilities to facilitate the subsequent analyses.

Figure 2 shows that both instabilities radiate internal inertial waves. They do so preferentially from the anticyclonic flanks, where the generating disturbance takes place. They also radiate preferentially away from the center of the jet, and are less likely to cross the cyclonic flank of the jet. We can form a hypothesis as to why by analogy with fluids where gravity, be it via stratification for internal waves or the free surface for Poincaré waves, plays a dominant role. As shown by e.g. Danioux *et al.* [29], in such systems, cyclones act as wave repellents and anticyclones as wave attractors, especially for waves whose frequencies are close to f. In our unstratified fluid, however, the situation is reversed: cyclonic regions attract waves and anticyclonic regions repel them. Indeed, the dispersion relation of inertial waves in a rotating, homogeneous fluid is $\omega^2 = F^2 \sin^2 \theta$, where ω is the angular frequency of the waves, $F = f\sqrt{1 + \mathrm{Ro}}$, and θ is the angle of the phase planes with respect to the direction of the rotation vector. Such inertial waves only exist where the fluid is stable, that is, where $1 + \mathrm{Ro} > 0$ and therefore where F is real. In such regions, $\omega < F$, with $F > f$ on the cyclonic flank, and vice-versa. Therefore, the cyclonic flank traps waves for which $f < \omega < F$ and forms a "cyclonic chimney", and by analogy with gravity-dominated

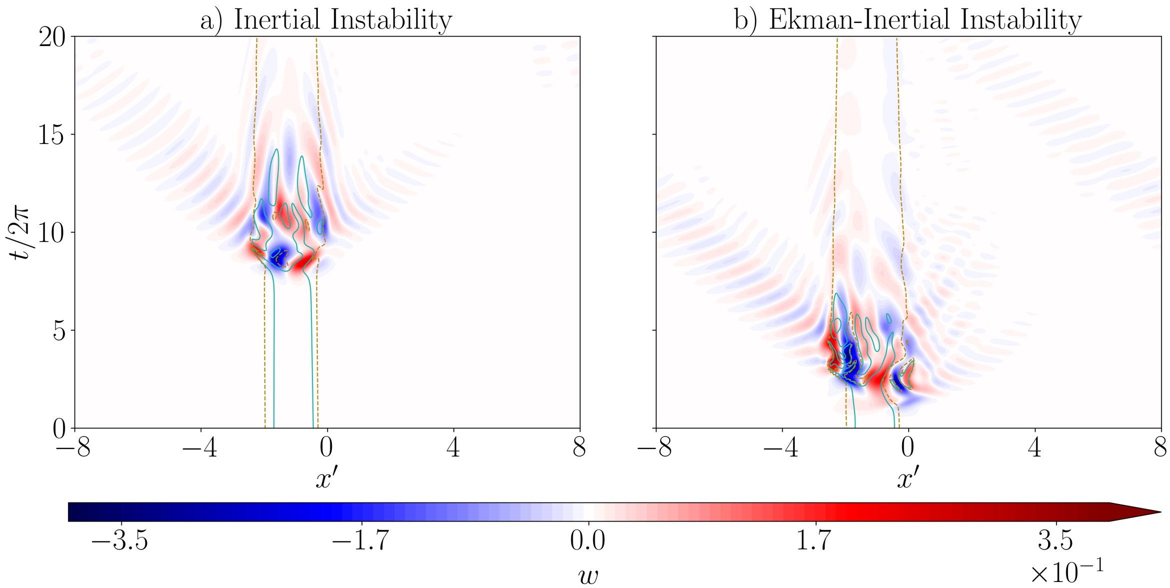

FIG. 2. Evolution of the vertical flow induced by InI and EII at $z = -0.5$ and for $\mathrm{Ro_{min}} = -1.5$, visualized in the reference frame of the inertial oscillation. Contours of $\mathrm{Ro} = -0.7$ and $\mathrm{Ro} = -1$ are shown in gold (dashed line) and turquoise (solid line), respectively.

fluids, we can hypothesize that the anticyclonic flank tends to repel waves. Validating these hypotheses would require a detailed analysis of the interactions between the waves and the mean flow, which we reserve for future studies. Also note that our "cyclonic chimneys" are the unstratified counterparts of the "anticyclonic chimneys" of gravity-dominated systems [30]. In such systems, F is the lower bound of ω in the dispersion relation, the upper bound being the buoyancy frequency.

2. Growth rate σ

Figure 3 highlights the differences in temporal evolution of growth rate σ for InI and EII for the sample simulation as hinted by the Hovmöller diagrams of vertical pumping in Figure 2. Because the magnitude of initial perturbations is essentially zero, the initial growth rate is approximately inversely proportional to the time step for both InI and EII. In the case of InI, the growth rate plummets to zero at $t/2\pi \approx 0.5$. This is consistent with the transient growth behavior, i.e., that of the intermediate state between the initial growth rate and long-term growth rate (e.g., exponential normal mode growth rate) [25, 31]. Since

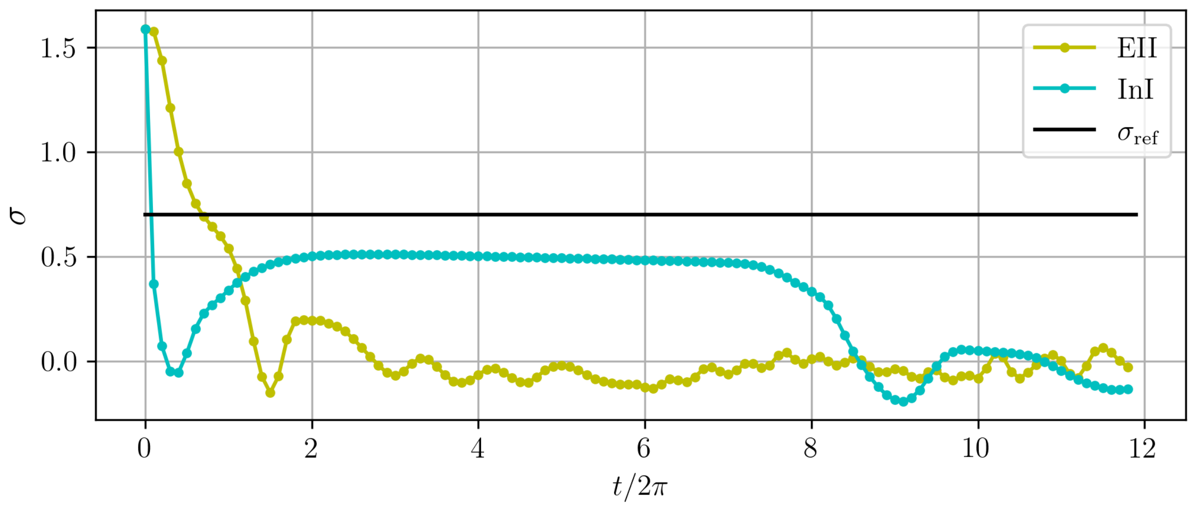

FIG. 3. Time series of the growth rate of InI and EII for the simulations with $\mathrm{Ro}_{\min} = -1.5$. The black line indicates the value of $\sigma_{\mathrm{ref}} = f\sqrt{-1 - \mathrm{Ro}_{\min}}$.

the initial growth rate is generally larger than the normal mode growth rate, the transient growth rate is expected to decrease over time. However, in the case of EII, the growth rate decreases much slower over the initial period, thus allowing the rapid development of instabilities and strong vertical flow as seen in Fig. 1(b) and Fig. 2(b).

The growth rate of InI exceeds the growth rate of EII around $t/2\pi = 1.2$. At $t/2\pi \approx 2$, the InI growth rate reaches its maximum of about 0.5. Note that the growth rate of perturbations in an inviscid, infinite-domain shear would be $\sigma_{\mathrm{ref}} = f\sqrt{-1 - \mathrm{Ro}_{\min}} \approx 0.7$. We attribute the discrepancy to the presence of vertical boundaries, finite lateral extent of the unstable region, and viscous effects, all of which reduce growth rates [24, 27]. The growth rate then starts decreasing slightly due to the slow viscous diffusion of the jet but remains relatively constant, and perturbations grow exponentially, according to linear theory. The instability starts saturating at about $t/2\pi = 7.5$, past which it abruptly drops to zero. After this point, similarly to EII, the growth rate remains close to zero.

3. Energetics

The energy budget of the system is calculated as in Eq. (5) for InI and EII, and each term is individually plotted in Figure 4. As each instability develops, some kinetic energy is naturally lost to dissipation. Note that in both cases, the minimum of the energy rate

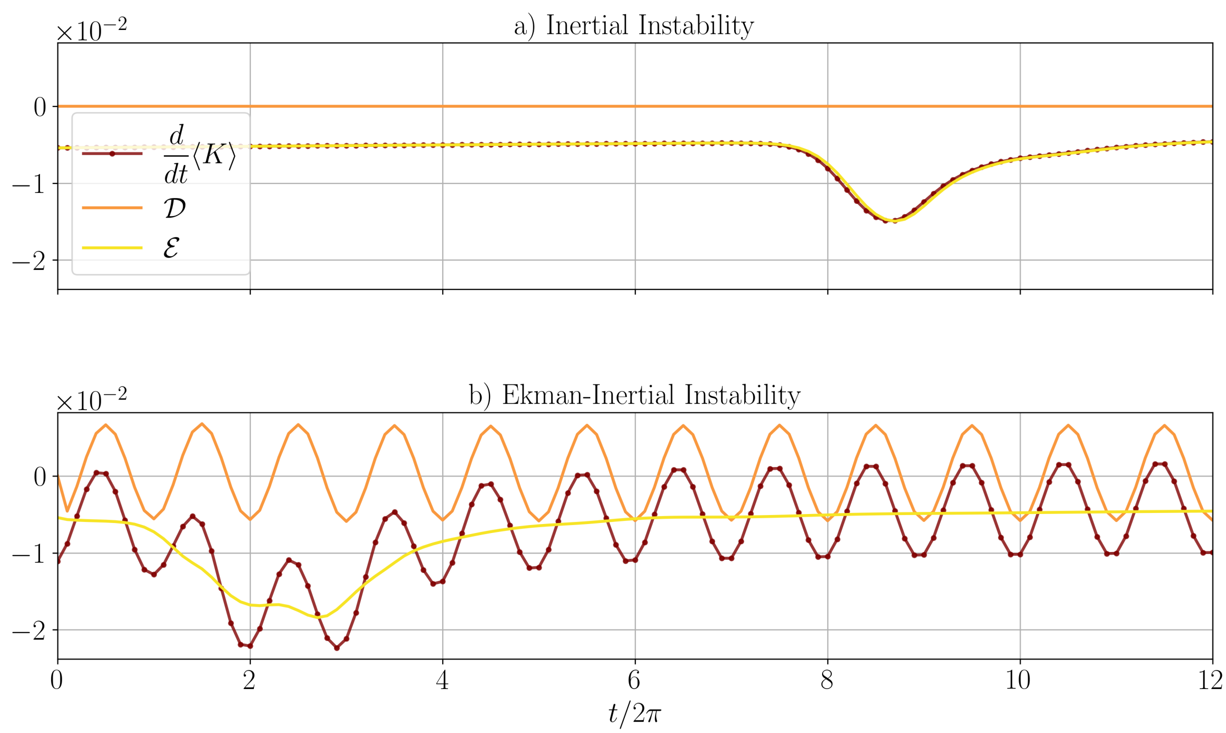

FIG. 4. Energy Budget of InI and EII at $\mathrm{Ro}_{\mathrm{min}} = -1.5$.

of change is reached once the instabilities start to weaken, that is, after their growth rate has also reached its minimum (see Figure 3), allowing enough time for the flow to dissipate kinetic energy. The most remarkable difference, however, is in the diffusion term of the energy budget; although it is negligible in InI, it shows an oscillating behavior in EII. Indeed, we apply constant wind stress on top of an inertial oscillation described in section II C, namely, a spatially-homogeneous horizontal flow of frequency close to f, whose direction is therefore constantly alternating with the direction of the wind forcing applied at the surface. Therefore, whenever the direction of the mean flow is the same (opposite) as the direction of the surface forcing, the diffusion of kinetic energy increases (decreases), leading to the oscillations observed in Figure 4.

4. *Vorticity statistics*

As both instabilities develop, the induced horizontal flow mixes cyclonic (stable) and anticyclonic (unstable) flow, leading to changes in the vorticity field. In Figure 5, each histogram represents the distribution of the local Rossby numbers at different times over

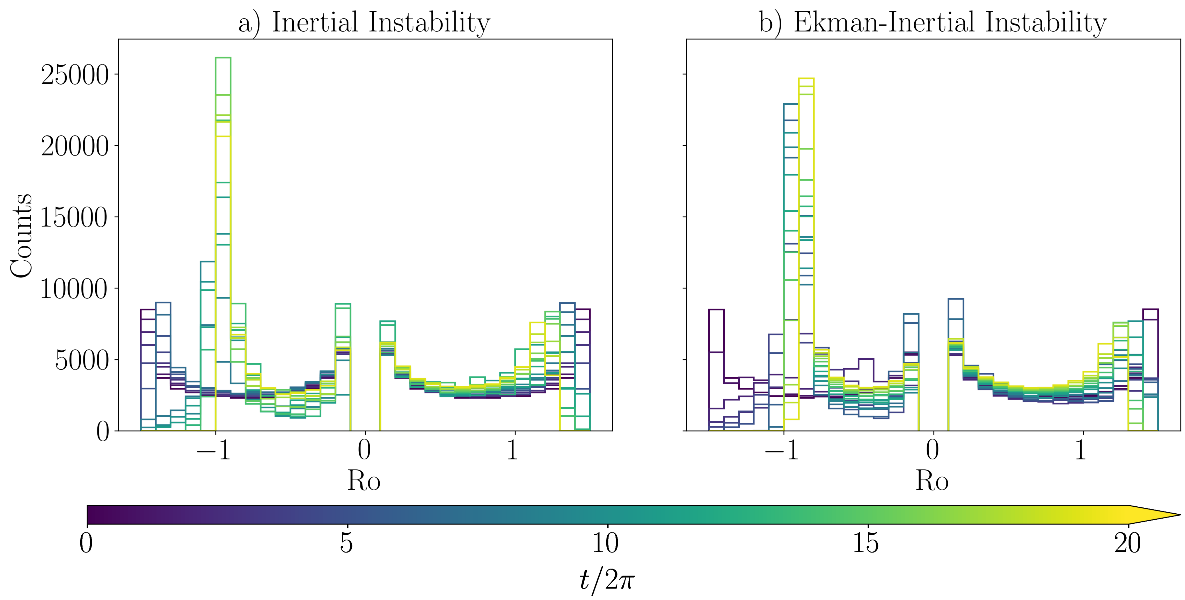

FIG. 5. Histograms of Ro at every inertial period, for a simulation with $\mathrm{Ro}_{\min} = -1.5$. To facilitate visualization, we do not show the sampling corresponding to the range $-0.1 < \mathrm{Ro} < 0.1$.

the course of the simulations. We exclude the range $-0.1 < \mathrm{Ro} < 0.1$ since the flanks of the current are characterized by $\mathrm{Ro} = 0$ at all times, but this is due to the Gaussian shape of the current, not the instabilities themselves. Note that the symmetry associated with the initial state of the current is eventually broken.

In the early stages of each instability, we observe a large peak at $\mathrm{Ro} = -1$. Over time, it shifts to a narrow peak around $-1 < \mathrm{Ro} < -0.7$, indicating that once the instabilities have subsided, much of the flow ends up close to the stability threshold. The main difference between the two is yet again in the timing: the process is much faster with EII than with InI, that is, stabilization occurs within $t/2\pi = 12$ in InI and $t/2\pi = 6$ in EII, which correspond to the times when kinetic energy rate of change reaches a steady state (Fig. 4) and the growth rate of perturbations is approximately zero (Fig. 3). After these times, we also do not find unstable flow in the Hovmöller diagrams of w (see turquoise lines in Fig. 2). Subsequently, both distributions remain in such a marginally stable state, with the EII maximum distribution slowly drifting towards higher values of Ro. While the post-instability evolution of the flow is beyond the scope of this work, we hypothesize that this drift is similar to the drift towards smaller values of Ro that we can see for the cyclonic distributions, and that these drifts are due to viscous diffusion smoothing out sharp velocity gradients.

B. Varying the minimal Rossby number

We investigate how the growth rates of EII and InI are affected by variations in $\mathrm{Ro}_{\mathrm{min}}$, i.e., changes in lateral shear of the flow. Figure 6 shows a time series of the growth rates, each line corresponding to a different experiment. While defining the InI growth rate is more straightforward because of its long-term modal growth, it is not obvious what value should be selected to be the representative growth rate from the EII experiments. Time series curves in Figure 6 reveal that the EII growth rate is more akin to that of transient growth in that it has an inherent time dependence and does not have the single value corresponding to the fastest-growing normal mode long-term behavior. In our simulations for both InI and EII, the initial growth rate is due to the non-normality of the initial condition, and the value is the same because all simulations have the same noisy initialization. Across all $\mathrm{Ro}_{\mathrm{min}}$ and for both InI and EII, the initial growth rate then reduces due to viscous forces at a similar rate for each instability type until $t/2\pi \approx 0.4$, indicated by the time series curves for each of InI- and EII-type simulations collapsing. The main difference is that InI growth rate is suppressed to zero, whereas EII sustains significantly positive growth rates. We, therefore, define the time period $t/2\pi \leq 0.4$ as the initial transient state and do not consider it in our analysis. For each $\mathrm{Ro}_{\mathrm{min}}$, we define the growth rate of InI to be the maximum growth rate after this transient initial period, which reveals the modal growth rate corresponding to the flat regions of the time series. As mentioned above, defining a single value for EII growth rate is more complicated. In this paper, we choose the growth rate values at $t/2\pi = 0.5$, acknowledging that this choice is somewhat arbitrary.

Interestingly, while the qualitative behavior of the EII growth rate remains rather similar across different values of $\mathrm{Ro}_{\mathrm{min}}$, the InI time series reveal a shorter phase of linear growth rate as $\mathrm{Ro}_{\mathrm{min}}$ becomes more negative. The relative dependence on $\mathrm{Ro}_{\mathrm{min}}$ is even more evident in Figure 7, which shows the maximum growth rate of each experiment as a function of $\mathrm{Ro}_{\mathrm{min}}$. Additionally, we show the theoretical maximum growth rate of InI, σ_{ref}, predicted by linear stability analysis. Because of viscous forces, InI growth rate is less than σ_{ref} for all values of $\mathrm{Ro}_{\mathrm{min}}$, similarly to what we observe in Figure 3. Notably, EII growth rate exceeds that of InI for all $\mathrm{Ro}_{\mathrm{min}}$ by a factor of $1.5-6$ and even exceeds σ_{ref} except for in the case of our most unstable jet with $\mathrm{Ro}_{\mathrm{min}} = -1.9$. The growth rates of both EII and InI increase with smaller (more unstable) $\mathrm{Ro}_{\mathrm{min}}$, but InI maximum growth rate varies more with $\mathrm{Ro}_{\mathrm{min}}$ than that of

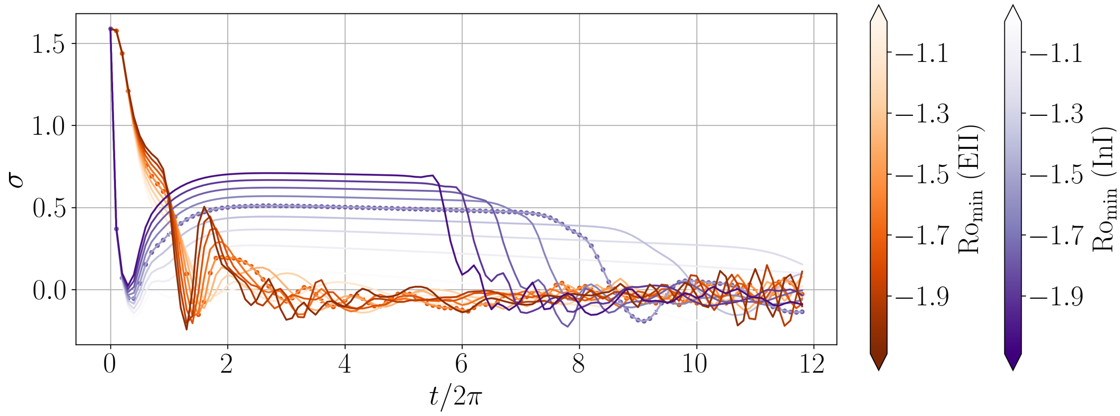

FIG. 6. Time series of growth rates for experiments with different $\mathrm{Ro}_{\mathrm{min}}$. We use markers to identify the time series from our sample $\mathrm{Ro}_{\mathrm{min}} = -1.5$ case and different colorbars to distinguish between the InI and EII experiments.

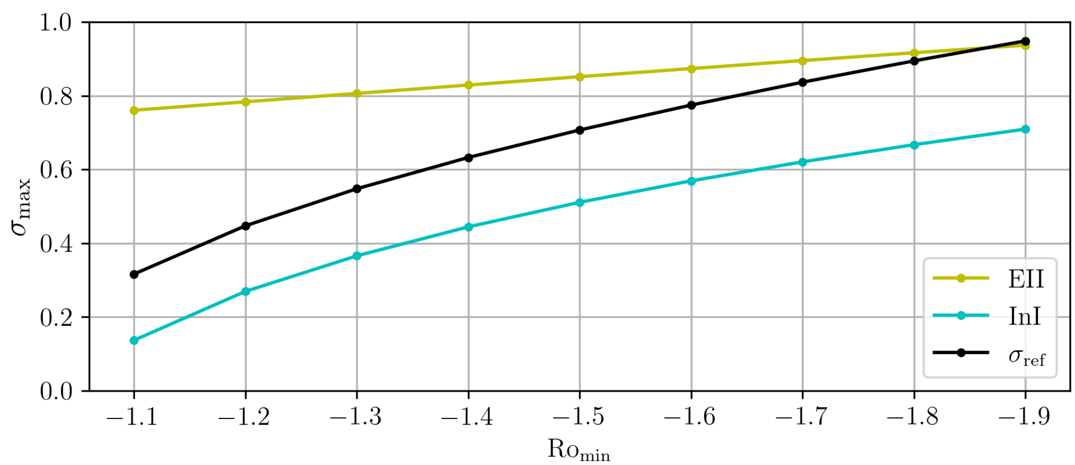

FIG. 7. Maximum growth rate for each instability, calculated after the transient state ($t/2\pi \geq 0.5$), as function of $\mathrm{Ro}_{\mathrm{min}}$. The black line corresponds to $\sigma_{\mathrm{ref}} = f\sqrt{-1 - \mathrm{Ro}_{\mathrm{min}}}$.

EII. Note that in EII, the imposed wind stress acts as the main triggering perturbation, and hence its growth rate might be more sensitive to other factors, such as the viscous forces responsible for its propagation.

IV. DISCUSSION AND CONCLUSIONS

The results of our idealized two-dimensional simulations qualitatively agree with some of the predictions by Grisouard and Zemskova [26], showing a significantly faster growth rate of EII compared to the growth rate of InI. Even though we find that EII growth rate exceeds that of InI by a factor of $1.5 - 6$, not by orders of magnitude as expected from the one-dimensional study [26], this primary difference still has dynamical consequences that become apparent in 2D, such that perturbations induce both horizontal and vertical flows that lead to turbulent motions and eventually extinguish the instability. The main conclusions of this work can be summarized as follows:

- EII grows faster than InI in the case of our step response to wind stress. The growth rate of EII is more time-dependent in contrast with a more easily identifiable long-term modal growth rate of InI.
- EII induces stronger horizontal and vertical flows and does so much earlier than InI.
- In both cases, the induced vertical flow is fast and strong enough to radiate inertial waves.
- In both instabilities, kinetic energy is lost to viscous dissipation and the emitted wave field. Additionally, the continuous surface forcing applied in EII diffuses kinetic energy throughout the entire simulation, but it does not significantly affect the global energy budget.
- EII manifests itself preferentially near the surface, while InI does so in the interior of the flow.
- Both instabilities reach a similar stable state, where most of the flow tends to remain close to the instability threshold $\mathrm{Ro} = -1$. This process occurs faster in EII than in InI.

In short, despite their common features, EII and InI have substantial differences that were not obvious from the one-dimensional analysis of Grisouard and Zemskova [26]. There are also important effects that our setup is not capturing, such as variations in the direction along the current and three-dimensional turbulence. Nevertheless, our work provides valuable information on the circulation induced in a plane across the current that results in vertical transport of ocean properties and can be more significant in EII than the one reported for other submesoscale instabilities.

Another limitation of our study is the assumption of homogeneous fluid, which is motivated by our focus on EII, whose main sources of kinetic energy are the lateral shear of the geostrophic current and the vertical shear provided by the surface forcing. This setup is also representative of the near-surface ocean mixed layer, where submesoscale instabilities are important. While this allows us to reveal the most basic dynamics of EII, a stratified environment would permit other submesoscale processes such as frontogenesis [32], mixed layer instabilities [15], or gravitational and/or symmetric instabilities [17]. Their effects might interfere with those of EII, resulting in either an enhancement or a reduction of vertical stratification and vertical velocities in the upper ocean.

For simplicity, we only consider the case of a constant wind stress along the current that starts at $t = 0$, or "infinitely" quickly, and is sustained throughout the simulation. Our motivation is that wind conditions can change much faster than surface currents, and trigger an EII-induced flow much faster than InI that grows in the interior of the domain. Nevertheless, how abrupt the surface forcing must be in order to trigger EII, and for it to outcompete InI or any of the aforementioned instabilities should be further investigated, as well as the sensitivity of EII to changes in the magnitude and direction of the wind.

In this study, we keep the Ekman number constant, which in dimensional quantities translates into keeping a fixed eddy viscosity ν. Since viscous fluxes are responsible for propagating the surface perturbation into the interior in the case of EII, we would expect variations in Ek to impact the vertical extent of the induced flow and its corresponding ability to dissipate kinetic energy. In this case, InI may become dominant below a "critical" depth given that it already starts within the interior of the flow. Such a hypothesis is testable using the configuration presented here, but is not the focus of this work.

Finally, the internal waves generated by both instabilities are of special interest. As shown in Figure 2, the most intense pumping is not centered in the domain. Instead, it develops mainly within the anticyclonic region, where the propagation of radiated waves is also enhanced, especially in EII, which is akin to the "inertial chimney" effect [29, 30]. Recall, however, that because our fluid is not stratified, our inertial chimneys are cyclonic. The fact that both instabilities emit internal waves shows that kinetic energy is exchanged between the original current that is initially in geostrophic balance and the wave field. A thorough analysis of such energetic interactions requires separating the balanced flow from the wave field, which can be achieved using several techniques, but is still a challenging task in fluid dynamics. Therefore, we will reserve the implementation of a Lagrangian filter that allows us to accurately conduct this separation and investigate the corresponding wave-mean flow interactions for a future study.

Data Availability Statement

The data that support the findings of this article will be publicly available upon publication.

ACKNOWLEDGMENTS

Computations were performed on the Béluga supercomputer located at the École de Technologie Supérieure in Montreal. F.T.J. acknowledges the financial support of the Consejo Nacional de Humanidades, Ciencias y Tecnologías (CONAHCYT) [doctoral scholarship number 774000]. F.T.J. and N.G. acknowledge the financial support of the Natural Sciences and Engineering Research Council of Canada (NSERC), [funding reference numbers RGPIN-2015-03684 and RGPIN-2022-04560]. V.E.Z. acknowledges the following National Science Foundation grants: OCE-1756752, OCE-2220439, and OCE-2319609.

---

[1] P. Klein, G. Lapeyre, L. Siegelman, B. Qiu, L.-L. Fu, H. Torres, Z. Su, D. Menemenlis, and S. Le Gentil, Ocean-scale interactions from space, Earth and Space Science **6**, 795 (2019).

[2] J. R. Taylor and A. F. Thompson, Submesoscale dynamics in the upper ocean, Annual Review of Fluid Mechanics **55**, 103 (2023).

[3] J. C. McWilliams, Submesoscale currents in the ocean, Proceedings of the Royal Society A: Mathematical, Physical and Engineering Sciences **472**, 20160117 (2016).

[4] L. Siegelman, Energetic submesoscale dynamics in the ocean interior, Journal of Physical Oceanography **50**, 727 (2020).

[5] Z. Su, J. Wang, P. Klein, A. F. Thompson, and D. Menemenlis, Ocean submesoscales as a key component of the global heat budget, Nature communications **9**, 1 (2018).

[6] K. M. Smith, P. E. Hamlington, and B. Fox-Kemper, Effects of submesoscale turbulence on ocean tracers, Journal of Geophysical Research: Oceans **121**, 908 (2016), https://agupubs.onlinelibrary.wiley.com/doi/pdf/10.1002/2015JC011089.

[7] M. Lévy, R. Ferrari, P. J. S. Franks, A. P. Martin, and P. Rivière, Bringing physics to life at the submesoscale, Geophysical Research Letters **39** (2012), https://agupubs.onlinelibrary.wiley.com/doi/pdf/10.1029/2012GL052756.

[8] M. Lévy, P. J. Franks, and K. S. Smith, The role of submesoscale currents in structuring marine ecosystems, Nature communications **9**, 4758 (2018).

[9] A. Mahadevan, The impact of submesoscale physics on primary productivity of plankton, Annual Review of Marine Science **8**, 161 (2016).

[10] J. R. Taylor and R. Ferrari, Ocean fronts trigger high latitude phytoplankton blooms, Geophysical Research Letters **38** (2011), https://agupubs.onlinelibrary.wiley.com/doi/pdf/10.1029/2011GL049312.

[11] Z. Jing, B. Fox-Kemper, H. Cao, R. Zheng, and Y. Du, Submesoscale fronts and their dynamical processes associated with symmetric instability in the northwest pacific subtropical ocean, Journal of Physical Oceanography **51**, 83 (2021).

[12] A. C. N. Garabato, X. Yu, J. Callies, R. Barkan, K. L. Polzin, E. E. Frajka-Williams, C. E. Buckingham, and S. M. Griffies, Kinetic energy transfers between mesoscale and submesoscale motions in the open ocean's upper layers, Journal of Physical Oceanography **52**, 75 (2022).

[13] R. Ferrari and C. Wunsch, Ocean circulation kinetic energy: Reservoirs, sources, and sinks, Annual Review of Fluid Mechanics **41**, 253 (2009).

[14] L. N. Thomas, A. Tandon, and A. Mahadevan, Submesoscale processes and dynamics, in *Ocean Modeling in an Eddying Regime* (American Geophysical Union (AGU), 2008) pp. 17–38, https://agupubs.onlinelibrary.wiley.com/doi/pdf/10.1029/177GM04.

[15] G. Boccaletti, R. Ferrari, and B. Fox-Kemper, Mixed layer instabilities and restratification, Journal of Physical Oceanography **37**, 2228 (2007).

[16] J. R. Taylor and R. Ferrari, Buoyancy and wind-driven convection at mixed layer density fronts, Journal of Physical Oceanography **40**, 1222 (2010).

[17] L. N. Thomas, J. R. Taylor, R. Ferrari, and T. M. Joyce, Symmetric instability in the gulf stream, Deep Sea Research Part II: Topical Studies in Oceanography **91**, 96 (2013), subtropical Mode Water in the North Atlantic Ocean.

[18] J. Gula, M. J. Molemaker, and J. C. McWilliams, Submesoscale cold filaments in the gulf stream, Journal of Physical Oceanography **44**, 2617 (2014).

[19] J. Callies, R. Ferrari, J. M. Klymak, and J. Gula, Seasonality in submesoscale turbulence, Nature communications **6**, 6862 (2015).

[20] L. Brannigan, D. P. Marshall, A. C. N. Garabato, A. J. G. Nurser, and J. Kaiser, Submesoscale instabilities in mesoscale eddies, Journal of Physical Oceanography **47**, 3061 (2017).

[21] N. Grisouard, Extraction of potential energy from geostrophic fronts by inertial–symmetric instabilities, Journal of Physical Oceanography **48**, 1033 (2018).

[22] V. Verma, H. T. Pham, and S. Sarkar, The submesoscale, the finescale and their interaction at a mixed layer front, Ocean Modelling **140**, 101400 (2019).

[23] T. W. N. Haine and J. Marshall, Gravitational, symmetric, and baroclinic instability of the ocean mixed layer, Journal of Physical Oceanography **28**, 634 (1998).

[24] G. F. Carnevale, R. C. Kloosterziel, and P. Orlandi, Journal of Fluid Mechanics **725**, 117–151 (2013).

[25] V. E. Zemskova, P.-Y. Passaggia, and B. L. White, Transient energy growth in the ageostrophic eady model, Journal of Fluid Mechanics **885**, A29 (2020).

[26] N. Grisouard and V. E. Zemskova, Ekman-inertial instability, Phys. Rev. Fluids **5**, 124802 (2020).

[27] M. Harris, F. Poulin, and K. Lamb, Inertial instabilities of stratified jets: Linear stability theory, Physics of Fluids **34** (2022).

[28] K. J. Burns, G. M. Vasil, J. S. Oishi, D. Lecoanet, and B. P. Brown, Dedalus: A flexible framework for numerical simulations with spectral methods, Phys. Rev. Res. **2**, 023068 (2020).

[29] E. Danioux, J. Vanneste, and O. Bühler, On the concentration of near-inertial waves in anticyclones, Journal of Fluid Mechanics **773**, R2 (2015).

[30] E. Kunze, Near-inertial wave propagation in geostrophic shear, Journal of Physical Oceanography **15**, 544 (1985).

[31] S. Kimura, Initial and transient growth of symmetric instability, Journal of Physical Oceanography **54**, 115 (2024).

[32] J. C. McWilliams, Oceanic frontogenesis, Annual Review of Marine Science **13**, 227 (2021).

[33] R. C. Kloosterziel, P. Orlandi, and G. F. Carnevale, Saturation of inertial instability in rotating planar shear flows, Journal of Fluid Mechanics **583**, 413 (2007).